SPECTRAL DISSIMILARITY BETWEEN MOMENTUM AND HEAT TRANSFERS IN TRANSITIONAL AND TURBULENT PLANE COUETTE FLOWS

Kengo Suetsugu
Graduate School of Mechanical Engineering
Shibaura Institute of Technology
Toyosu 3-7-5, Tokyo, 135-8548 Japan
email: aa20001@shibaura-it.ac.jp

Takahiro Tsukahara
Department of Mechanical and Aerospace Engineering, Tokyo University of Science
Yamazaki 2641, Chiba, 278-8510 Japan
email: tsuka@rs.tus.ac.jp

Takuya Kawata
Department of Advanced Mechanical Engineering
Shibaura Institute of Technology
Toyosu 3-7-5, Tokyo, 135-8548 Japan
email: kawata@shibaura-it.ac.jp

ABSTRACT

Nonlinear interactions between different scales in turbulence play an important role in momentum transport in turbulence and are also crucial in turbulent heat transfer. Despite both phenomena are similar in several characteristics, they are also dissimilar in spectral feature. In this study, we perform direct numerical simulations of plane Couette turbulence with passive scalar heat transfer under various Reynolds and Prandtl number conditions to investigate the Reynolds- and Prandtl-number dependencies of spectral dissimilarities between turbulent heat and momentum transfers. The results show that turbulent heat transfer tends to occur at relatively smaller scales compared to momentum transfer, and the ratio between representative wavelengths of turbulent heat and momentum transfers displays both Reynolds and Prandtl number dependencies. The scale dissimilarity becomes more pronounced with increasing Reynolds number, while it exhibits a non-monotonic dependency on the Prandtl number, showing most significant dissimilarity at relatively low Prandtl number around $Pr = 0.5$.

INTRODUCTION

Nonlinear interaction between different scales is an important aspect of turbulence, by which turbulent energy is redistributed between different scales and spatial diffusions of momentum and heat are significantly enhanced. In particular, the effect of turbulent mixing and diffusion of momentum and heat results in a substantial increase in friction drag and heat transfer on the wall. Therefore, the possibility of their dissimilar control, i.e., simultaneous achievement of momentum transfer suppression and heat transfer enhancement, has long been of great interest in turbulence research from an engineering point of view.

Wall-bounded turbulent flows are characterized by multi-scale vortical structures including relatively small-scale coherent structures in the near-wall region and large-scale structures located in the logarithmic region or further away from the wall. It is, therefore, important to understand how these flow structures at different scales interact with each other and how such scale interactions result in the momentum and heat transfer in wall turbulence. In recent years, there have been intensive efforts to study the role of scale interactions in turbulent kinetic energy transfer in wall turbulence (see, for example, Cimarelli *et al.*, 2016; Mizuno, 2016; Lee & Moser, 2019; Chiarini *et al.*, 2022, etc.), but not much for heat transfers.

In our previous study (Kawata & Tsukahara, 2022), we investigated the spectra of the turbulent momentum and heat transfers in a plane Couette turbulence by means of direct numerical simulation (DNS), and showed that the heat transfer spectrum exhibits the peak at a relatively short streamwise wavelength as compared to the momentum transfer spectrum. This indicates that fluid motions related to the increase of the wall heat flux are at relatively smaller streamwise length scales than those related to the increase of wall shear stress. This observation of spectral dissimilarity between momentum and heat transfer is certainly interesting, but the study was limited to at the friction Reynolds number $Re_\tau = 126.1$ and $Pr = 0.71$. In this study, we perform DNS of plane Couette turbulences at several different Reynolds and Prandtl number conditions in order to investigate the Reynolds- and Prandtl-number dependency of the scale dissimilarity of momentum and heat transfers. We show that the scale dissimilarity becomes more pronounced with increasing Reynolds number, while its Prandtl-number dependency is non-monotonic, with the most significant dissimilarity found at relatively low Prandtl number around $Pr = 0.5$.

DIRECT NUMERICAL SIMULATION

The plane Couette flow considered in the present DNS is driven by shear by two flat plates; the distance between them is h, the bottom plate is stationary and the top one is translating with a constant velocity U_w. The x-, y- and z-axes denote the streamwise, wall-normal and spanwise directions, respectively, and the origin of the coordinates is placed on the bottom

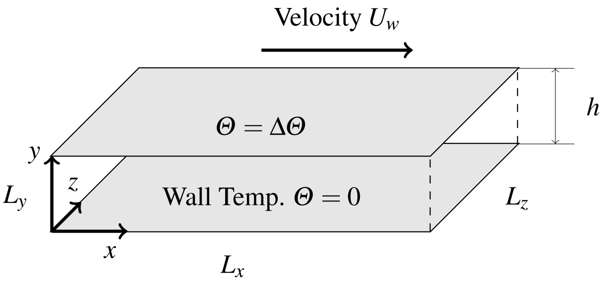

Figure 1. Geometrical configuration of DNS

wall. The temperatures on the walls are uniform and constant in time with the temperature difference $\Delta\Theta$ (the temperature of the top wall is higher by $\Delta\Theta$).

The governing equations for the velocity and scalar temperature fields are the non-dimensional continuity and Navier-Stokes equations for incompressible fluid flow:

$$\frac{\partial u_i^*}{\partial x_i^*} = 0, \tag{1a}$$

$$\frac{\partial u_i^*}{\partial t^*} + u_k^* \frac{\partial u_i^*}{\partial x_k^*} = -\frac{\partial p^*}{\partial x_i^*} + \frac{1}{Re_{\mathrm{w}}} \frac{\partial^2 u_i^*}{\partial x_k^{*2}}, \tag{1b}$$

and a transport equation of a scalar temperature θ:

$$\frac{\partial \theta^*}{\partial t^*} + u_k^* \frac{\partial \theta^*}{\partial x_k^*} = \frac{1}{Pr Re_{\mathrm{w}}} \frac{\partial^2 \theta^*}{\partial x_k^{*2}}. \tag{1c}$$

The above equations are scaled based on U_{w}, h or/and $\Delta\Theta$, and the superscript * denotes instantaneous non-dimensional quantities. The Reynolds number and the Prandtl number are defined as $Re_{\mathrm{w}} = U_{\mathrm{w}} h/\nu$ and $Pr = \nu/\alpha$, where ν and α are the kinematic viscosity and thermal diffusivity of the fluid, respectively. The periodic boundary condition is applied for x- and z-directions for both velocity and temperature fields. As for the boundary conditions on the walls, non-slip condition and constant-temperature-difference condition are adopted for velocity and temperature fields, respectively:

$$\begin{cases} \text{At } y^* = 1,\ (u^*, v^*, w^*) = (1,\,0,\,0),\ \theta^* = 1, \\[2ex] \text{At } y^* = 0,\ (u^*, v^*, w^*) = (0,\,0,\,0),\ \theta^* = 0. \end{cases} \tag{2}$$

The governing equations (1a) and (1c) are solved by the same numerical schemes as those used by Tsukahara *et al.* (2006), where the velocity and temperature fields are solved in physical space with the finite difference method, while the pressure Poisson equation is solved in Fourier space. The central difference schemes with the fourth and second order are used for the wall-parallel (x- and z-) and -normal (y-) directions, respectively.

We have run seven DNS cases with different Re_{w} and Pr for the range 4,300$\leq Re_{\mathrm{w}} \leq$19,000 and $0.1 \leq Pr \leq 4$, as listed in Table 1. The Case-Ref is the reference case from our previous study (Kawata and Tsukahara, 2022), where a relatively large computational domain ($L_x = 24h$, $L_z = 12.8h$) was used to perform a DNS at $Re_{\mathrm{w}} = 8,600$ and $Pr = 0.71$. In the present study, on the other hand, smaller computational domains with $L_x = 9.14h$ and $L_z = 4h$ are used to reduce

Table 1. DNS cases simulated in the present study and the computational conditions. The obtained friction Reynolds number Re_τ and the resultant grid resolutions. The Case-Ref is the reference computation performed by Kawata & Tsukahara (2022).

Case	Re_{w}	Pr	$N_x \times N_y \times N_z$	Re_τ
R43P1	4,300	1.0	$2^8 \times 96 \times 2^8$	69.9
R86P01	8,600	0.1	$2^8 \times 96 \times 2^8$	126.8
R86P05	8,600	0.5	$2^8 \times 96 \times 2^8$	125.7
R86P1	8,600	1.0	$2^8 \times 96 \times 2^8$	125.7
R86P2	8,600	2.0	$2^9 \times 192 \times 2^9$	122.3
R86P4	8,600	4.0	$2^9 \times 192 \times 2^9$	127.7
R190P1	19,000	1.0	$2^9 \times 192 \times 2^9$	256.2
Ref	8,600	0.71	$2^9 \times 96 \times 2^9$	126.1

computational cost for each case. We have confirmed that the statistical quantities related to the velocity field, such the Reynolds stresses and their spectra, obtained in Case-Re86Pr1 are in a qualitative agreement with those obtained by Case-Ref, suggesting that the effect of relatively small domain does not qualitatively affect the turbulent velocity field obtained in the present DNS (note here that the temperature field is passive to the velocity field). The number of computational grids in each case is determined to retain sufficient spatial resolutions: $\Delta x^+ \sqrt{Pr} \sim 4$ – 10, $\Delta y_{\mathrm{min}} \sqrt{Pr} \sim 0.1$ and $\Delta z \sqrt{Pr} \sim 4$ (here the superscript $^+$ denotes the values scaled based on the wall units).

In the present study, we denote the instantaneous velocities and temperature as $u_i = U_i + u_i'$ and $\theta = \Theta + \theta'$, where the uppercase letters $U_i = \langle u_i \rangle$ and $\Theta = \langle \theta \rangle$ denote the mean values averaged in the x- and z-directions and in time, and the lowercase letters with $'$ are the fluctuations from the mean values. The friction Reynolds number $Re_\tau = u_\tau \delta/\nu$ (u_τ is the friction velocity and $\delta = 0.5h$ is the channel half height) is evaluated from the obtained mean velocity profiles, and the value in each case is also presented in Table 1.

RESULTS AND DISCUSSIONS

Figure 2 presents the distributions of the streamwise spectra of the Reynolds shear stress E_{-uv} and turbulent heat flux $E_{-v\theta}$, which are defined as

$$E_{-uv}(y, k_x) = -2\mathscr{R}\left(\left\langle \widetilde{u}(k_x)\widetilde{v}^\dagger(k_x)\right\rangle\right), \tag{3a}$$

$$E_{-v\theta}(y, k_x) = -2\mathscr{R}\left(\left\langle \widetilde{v}(k_x)\widetilde{\theta}^\dagger(k_x)\right\rangle\right), \tag{3b}$$

where $\widetilde{u}_i(k_x)$ and $\widetilde{\theta}(k_x)$ are the Fourier coefficients of u_i' and θ', respectively, at the streamwise wavenumber k_x, and the superscript † and $\mathscr{R}$ denote the conjugates and the real parts of complex quantities, respectively. The distributions are presented in the premultiplied form as functions of the wall-normal position y and the streamwise wavelength $\lambda_x = 2\pi/k_x$, and are compared for three different Reynolds numbers $Re_{\mathrm{w}} = 4300$, 8600 and 19000 at the Prandtl number $Pr = 1$. It is shown in Fig. 2(a) that as the Reynolds number increases the Reynolds shear stress spectrum $k_x E_{uv}$ becomes more concentrated and shifts toward shorter wavelengths, particularly in the near-wall

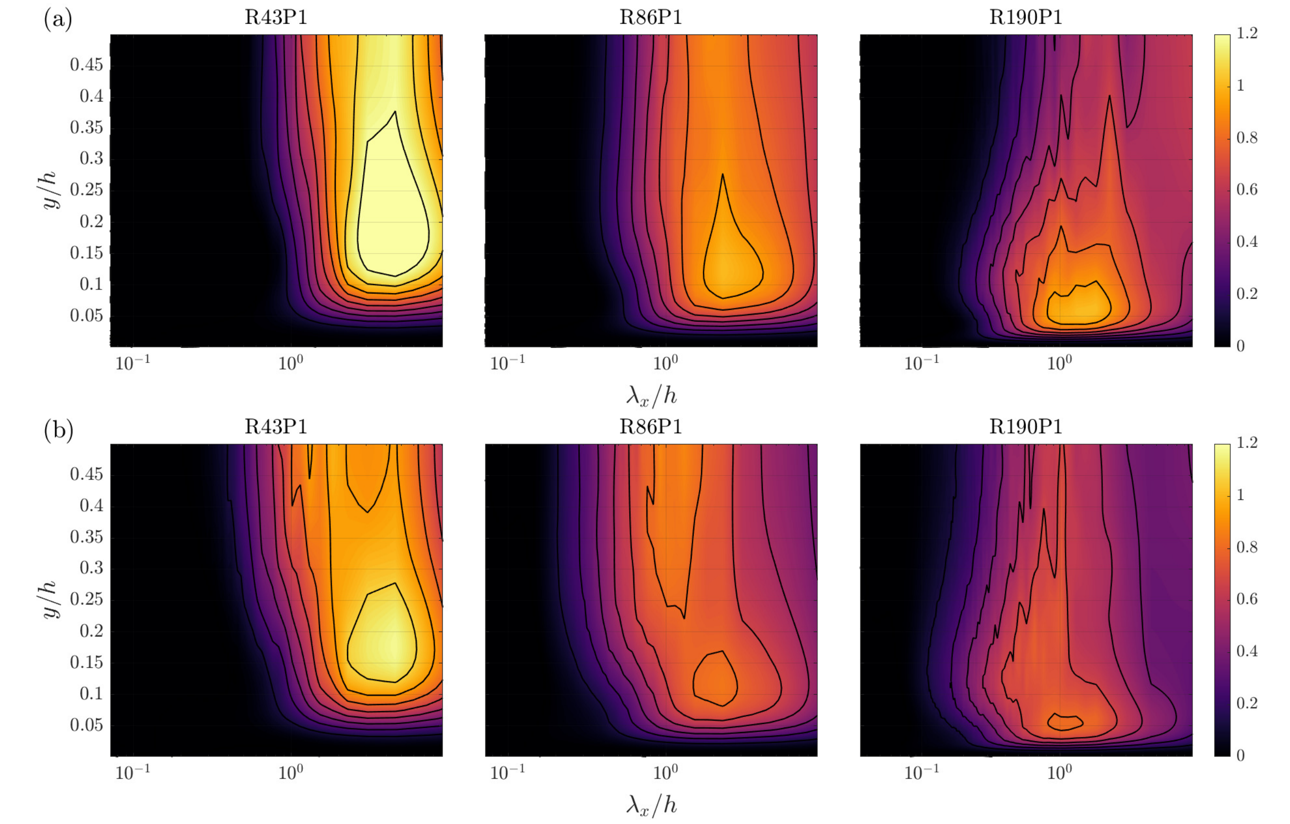

Figure 2. Distributions of premultiplied spectra of (a) Reynolds shear stress $k_x E_{-uv}$ and (b) turbulent heat flux $k_x E_{-v\theta}$ at three different Reynolds numbers $Re_\mathrm{w} = 4300$, 8600 and 19000 with $Pr = 1$. The values of $k_x E_{-uv}$ and $k_x E_{-v\theta}$ are scaled by the maximum values of $-\langle u'v' \rangle$ and $-\langle v'\theta' \rangle$ in each case, respectively.

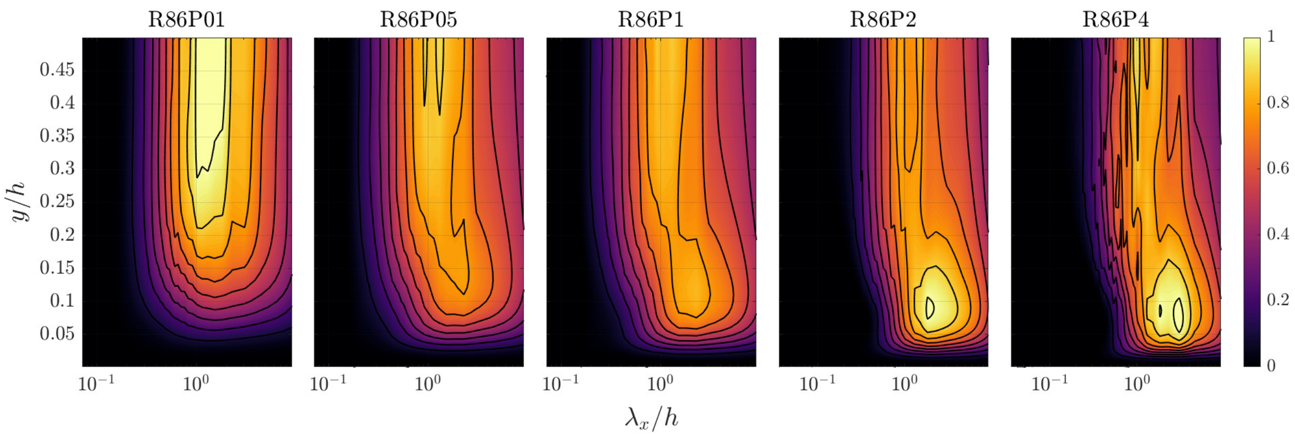

Figure 3. Distributions of premultiplied spectra of turbulent heat flux $k_x E_{-v\theta}$ at five different Prandtl numbers $Pr = 0.1, 0.5, 1, 2, 4$ with $Re_\mathrm{w} = 8600$. The values are scaled by the maximum values of $-\langle v'\theta' \rangle$ in each case.

region, where the peak corresponding to the coherent structure in the inner layer becomes pronounced with increasing Re_w. Particularly at the lowest Reynolds number $Re_\mathrm{w} = 4,300$ the distribution of $k_x E_{-uv}$ appears relatively broad in the y-direction, extending from the near-wall to the central region of the channel, and the distinct energy peak near the wall, which is clearly observed at higher Reynolds numbers, is not observed. This indicates that the near-wall structures and the very large-scale structure of the plane Couette turbulence are not clearly separated at this low Re_w. The turbulent heat flux spectrum $k_x E_{-v\theta}$ exhibits, as shown in Fig. 2(b), a similar trend to the Reynolds shear stress spectrum $k_x E_{-uv}$, with the spectral energy shifting toward smaller scales as the Reynolds number increases. However, the shift is more pronounced in the turbulent heat flux spectrum $k_x E_{v\theta}$ than in the Reynolds shear stress spectrum $k_x E_{-uv}$, especially in the central region of the channel, indicating that turbulent heat transfer is more sensitive to small-scale turbulence.

Figure 3 compares the distributions of the turbulent heat flux spectrum at five different Prandtl number ranging $0.1 \leq Pr \leq 4$ with $Re_\mathrm{w} = 8600$. Note here that the Reynolds shear stress spectrum $k_x E_{-uv}$ corresponding to these distributions of $k_x E_{-v\theta}$ is that in Case R86P1 presented in Fig. 2(a), as the Reynolds number is $Re_\mathrm{w} = 8600$ for all these five cases. As shown in Fig. 3, the contribution by the near-wall peak of the $k_x E_{-v\theta}$ distribution are more pronounced as Pr increases. On the other hand, the near-wall peak disappears at the lowest Prandtl number case $Pr = 0.1$, and $E_{-v\theta}$ is significant at relatively short wavelengths in the channel core region. This tendency seems to be correspond to the known turbulent heat flux profile in channel or Couette flow which presents higher Prandtl number condition have its peak closer to the wall (Abe *et al.*, 2004).

Now, we quantify the scales of turbulent fluid motions that are mainly responsible to each wall shear stress and wall heat flux based on the distributions of the spectra of the Reynolds shear stress and turbulent heat flux presented in Figs. 2 and 3. The wall shear stress τ_{w} and the wall heat flux q_{w} are decomposed to their laminar-case values—$\tau_{\mathrm{w,lam}}$ and $q_{\mathrm{w,lam}}$—and the increases from them by the additional momentum and heat transfers due to turbulent motions—$\Delta\tau_{\mathrm{w,tur}}$ and $\Delta q_{\mathrm{w,tur}}$—as

$$\tau_{\mathrm{w}} = \underbrace{\mu \frac{U_{\mathrm{w}}}{h}}_{\tau_{\mathrm{w,lam}}} + \underbrace{\int_0^h -\langle u'v' \rangle \,\mathrm{d}y}_{\Delta\tau_{\mathrm{w,tur}}}, \tag{4a}$$

$$q_{\mathrm{w}} = \underbrace{\kappa \frac{\Delta\Theta}{h}}_{q_{\mathrm{w,lam}}} + \underbrace{\int_0^h -\langle v'\theta' \rangle \,\mathrm{d}y}_{\Delta q_{\mathrm{w,tur}}}, \tag{4b}$$

where μ and κ are the dynamic viscosity and thermal conductivity of the fluid, respectively. The above equations indicate that the Reynold shear stress $-\langle u'v' \rangle$ and the turbulent heat flux $\langle -v'\theta' \rangle$ are directly related to the increase of the wall shear stress and the wall heat flux, respectively, from their laminar-case values. As the Reynolds shear stress $-\langle u'v' \rangle$ and the turbulent heat flux $-\langle v'\theta' \rangle$ are the integrals of E_{-uv} and $E_{-v\theta}$, respectively, the turbulent part of the wall shear stress and the wall heat flux are expressed in terms of the spectral quantities as follows:

$$\Delta\tau_{\mathrm{w,tur}} = \int_{-\infty}^{\infty} \mathscr{E}_{-uv}(k_x) dk_x, \tag{5a}$$

$$\Delta q_{\mathrm{w,tur}} = \int_{-\infty}^{\infty} \mathscr{E}_{-v\theta}(k_x) dk_x, \tag{5b}$$

where $\mathscr{E}_{-uv}$ and $\mathscr{E}_{-v\theta}$ be the turbulent momentum-transfer spectrum and the turbulent heat-transfer spectrum, respectively, which are defined by integrating the Reynolds shear stress spectrum E_{-uv} and the turbulent heat flux spectrum $E_{-v\theta}$ across the channel as

$$\mathscr{E}_{-uv}(k_x) = \frac{1}{h} \int_0^h E_{-uv}(y, k_x) dy, \tag{6a}$$

$$\mathscr{E}_{-v\theta}(k_x) = \frac{1}{h} \int_0^h E_{-v\theta}(y, k_x) dy. \tag{6b}$$

Equations (5) show that $\mathscr{E}_{-uv}$ and $\mathscr{E}_{-v\theta}$ are the spectral contents of $\tau_{\mathrm{w,tur}}$ and $q_{\mathrm{w,tur}}$, respectively, and therefore evaluating $\mathscr{E}_{-uv}$ and $\mathscr{E}_{-v\theta}$ enables us to investigate the scales of turbulent fluid motions that are directly related to increase of wall shear stress and wall heat flux.

By integrating the distributions of $k_x E_{-uv}$ and $k_x E_{-v\theta}$ presented in Fig. 2 in the y-direction, we obtain the profiles of the premultiplied turbulent momentum transfer spectrum $k_x \mathscr{E}_{-uv}$ and the premultiplied turbulent heat transfer spectrum $k_x \mathscr{E}_{-v\theta}$

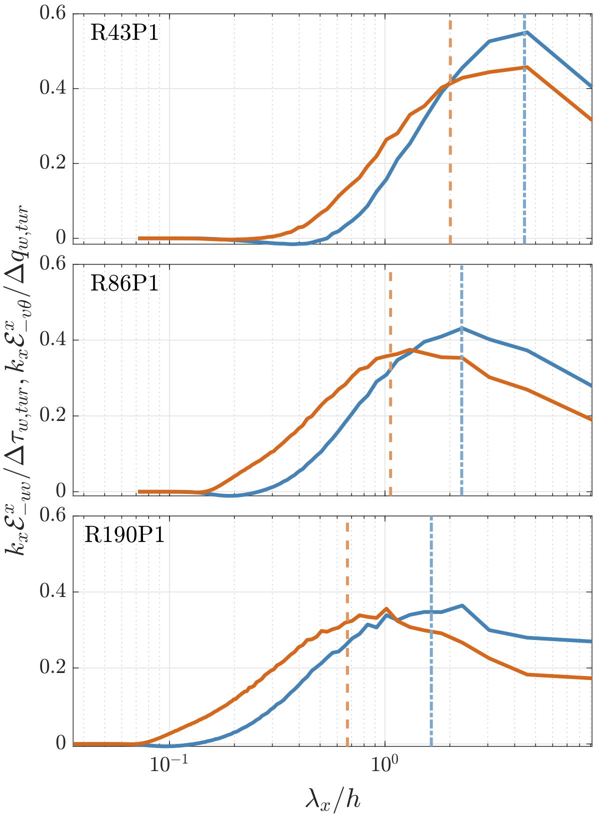

Figure 4. Comparison of normalized premultiplied spectra of (blue) turbulent momentum transfer $k_x \mathscr{E}^x_{-uv}$ and (red) turbulent heat transfer $k_x \mathscr{E}^x_{-v\theta}$ at different Re_{w} with $Pr = 1$: (R43P1) $Re_{\mathrm{w}} = 4{,}300$, (R86P1) $Re_{\mathrm{w}} = 8{,}600$, and (R190P1) $Re_{\mathrm{w}} = 19{,}000$. The vertical dashed lines in each panel indicate representative wavelengths of (blue) momentum transfer $\lambda_{x,M}$ and (red) heat transfer $\lambda_{x,H}$.

at $Pr = 1$ with three different Reynolds numbers, which are compared in Fig. 4. As shown, both profiles of $k_x \mathscr{E}_{-uv}$ and $k_x \mathscr{E}_{-v\theta}$ exhibit broad profiles with a peak located at wavelengths on the order of $\lambda_x/h \approx 1$, and the peak wavelengths are shown to decreases with increasing Re_{w}. These changes of the peak locations correspond to the Reynolds-number dependency of the distributions of the premultiplied spectra $k_x E_{-uv}$ and $k_x E_{-v\theta}$ investigated in Fig. 2; as the Reynolds number increases, both distributions of $k_x E_{-uv}$ and $k_x E_{-v\theta}$ shift overall toward shorter wavelengths, and their near-wall peak locations also move closer to the wall and toward shorter wavelengths. The striking feature found here is that comparing the profiles of $k_x \mathscr{E}_{-uv}$ and $k_x \mathscr{E}_{-v\theta}$ for each Re_{w} case the $k_x \mathscr{E}_{-v\theta}$ profile is somewhat shifted towards shorter wavelengths as compared to the $k_x \mathscr{E}_{-uv}$ profile in all Re_{w} cases, confirming the same tendency as observed by Kawata & Tsukahara (2022) at $Re_{\mathrm{w}} = 8600$ and $Pr = 0.71$ for the other Prandtl number $Pr = 1.0$ and three different Re_{w} this time. This shift of the $\mathscr{E}_{-v\theta}$ profile to the shorter λ_x side implies that turbulent heat transfer occurs certainly smaller (streamwise) length scales than momentum transfers. It also appears that the dissimilarity between the $\mathscr{E}_{-uv}$ and $\mathrm{E}_{-v\theta}$ profiles becomes more notable as Re_{w} increases.

To further investigate the Reynolds number dependency of the dissimilarity between the turbulent momentum and heat transfer spectra, we have run an additional computation for the case at a very low Reynolds number $Re_{\mathrm{w}} = 1500$ with

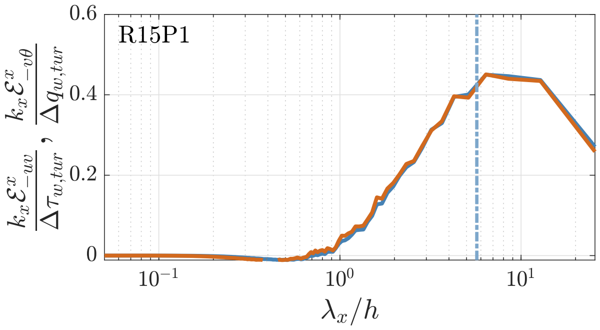

Figure 5. Comparison of normalized premultiplied turbulent momentum and heat transfer spectra under the turbulent stripe condition: $Re_\mathrm{w} = 1,500$ and $Pr = 1$. The solid and vertical dashed lines indicate the same as in Fig. 4.

$Pr = 1$ (R15P1), where turbulence is intermittent and a turbulent stripe structure appears (see, for example, Tsukahara *et al.*, 2005). To capture the very large-scale laminar–turbulent pattern of the turbulent stripe, a larger computation domain ($L_x \times L_y \times L_z = 51.2h \times h \times 25.6h$, $Nx \times Ny \times Nz = 1024 \times 96 \times 512$) was employed. Figure 5 presents the profiles of $k_x\mathscr{E}_{-uv}$ and $k_x\mathscr{E}_{-v\theta}$ obtained in this case, which exhibits no dissimilarity between the spectra of turbulent momentum and heat transfers.

We also investigate the Prandtl-number dependency of the turbulent heat transfer spectrum $\mathscr{E}_{-v\theta}$. Figure 6 presents the profiles of $k_x\mathscr{E}_{-uv}$ and $k_x\mathscr{E}_{-v\theta}$ at $Re_\mathrm{w} = 8600$ and five different Pr. Note here that the profiles of $k_x\mathscr{E}_{v\theta}$ in each case is obtained by integrating the corresponding $k_xE_{-v\theta}$ distribution presented in Fig. 3, and the profiles of $k_x\mathscr{E}_{-uv}$ are all nearly identical to each other (they are slightly differ from each other although simulating statistically same flows, because the spatial resolutions and time steps are somewhat different in each computation corresponding to different Pr). As can bee seen in Fig. 6, all Prandtl number cases exhibit the dissimilarity between the turbulent momentum and heat transfer spectra—the shifts of $\mathscr{E}_{-v\theta}$ profiles in shorter wavelengths—consistently indicating that heat transfer by turbulence occurs relatively smaller streamwise length scales than momentum transfer. The difference between the profiles of $\mathscr{E}_{-uv}$ and $\mathscr{E}_{-v\theta}$ appears to be especially notable at $Pr = 0.5$ and $Pr = 1$.

In order to quantify the scales of the turbulent structures that are mainly responsible to momentum and heat transfer, we define the representative wavenumbers for eahc turbulent momentum and heat transfer based on the profiles of $\mathscr{E}_{-uv}$ and $\mathscr{E}_{-v\theta}$ as follows:

$$M_x(Re_\mathrm{w}, Pr) = \frac{\int_{-\infty}^{\infty} k_x\mathscr{E}_{-uv}(k_x)\mathrm{d}k_x}{\int_{-\infty}^{\infty} \mathscr{E}_{-uv}(k_x)\mathrm{d}k_x}, \tag{7a}$$

$$H_x(Re_\mathrm{w}, Pr) = \frac{\int_{-\infty}^{\infty} k_x\mathscr{E}_{-v\theta}(k_x)\mathrm{d}k_x}{\int_{-\infty}^{\infty} \mathscr{E}_{-v\theta}(k_x)\mathrm{d}k_x}. \tag{7b}$$

The streamwise length scales based on the above-defined wavenumbers—$\lambda_{x,M} = 2\pi/M_x$ and $\lambda_{x,H} = 2\pi/H_x$—can be interpreted as the integral streamwise length scales related to each momentum and heat transfers.

The vertical dashed lines in Figs. 4, 5 and 6 indicate (blue) $\lambda_{x,M}$ and (red) $\lambda_{x,H}$ in each case. As shown in Fig. 4, both $\lambda_{x,M}$ and $\lambda_{x,H}$ clearly decreases as Re_w increases, indicating that both length scales related to momentum and heat transfers become smaller with increasing Re_w as generally expected. It is shown in Fig. 6 that $\lambda_{x,M}$ decreases as Pr decreases from $Pr = 4$ to $Pr = 0.5$, indicating that the scales related to turbulent heat transfer becomes smaller with decreasing Pr. This variation of the representative wavelength for heat transfer corresponds to the disappearance of the near-wall peak of the $k_xE_{-v\theta}$ distributions with decreasing Pr, as shown in Fig. 3. The lowest Prandtl number case Case R86P01 seems not following this trend, exhibiting a almost same value of $\lambda_{x,H}$ as than that in the case at $Pr = 0.5$. This is probably because the near-wall peak in the $k_xE_{-v\theta}$ distribution has already almost vanished in the case of $Pr = 0.5$ and therefore those distributions of $k_xE_{-v\theta}$ at $Pr = 0.5$ and $Pr = 0.1$ have little difference in their integrated quantities.

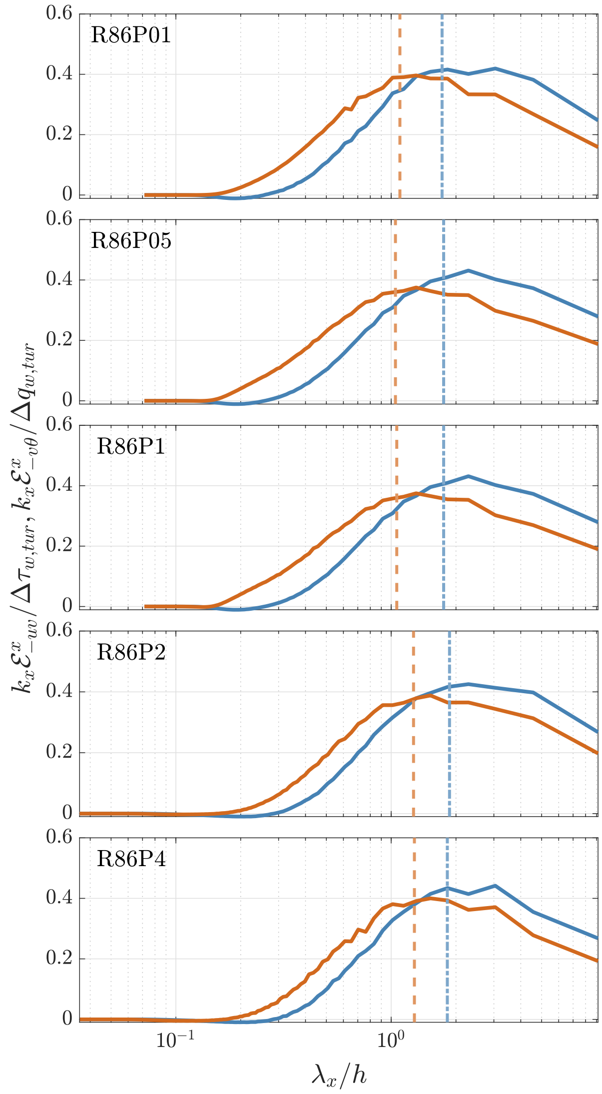

Figure 6. Comparison of normalized premultiplied spectra of (blue) turbulent momentum transfer $k_x\mathscr{E}^x_{-uv}$ and (red) heat transfer $k_x\mathscr{E}^x_{-v\theta}$ at different Re_w and Pr: (b1–b5) at $Pr = 0.1, 0.5, 1, 2$ and 4 with $Re_\mathrm{w} = 8,600$. The dashed lines in each panel indicate representative wavelengths $\lambda_{x,M}$ and $\lambda_{x,H}$.

Now we quantify the degree of dissimilarity between the length scales associated with momentum and heat transfers as the wavelength ratio $\lambda_{x,H}/\lambda_{x,M}$. The variations of this wavelength ratio with Re_w and Pr are presented in Fig. 7. It is shown here that, within the parameter range investigated in

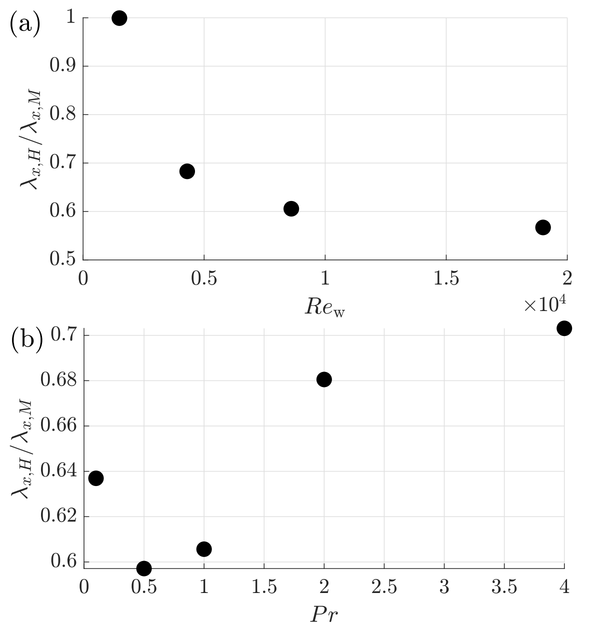

Figure 7. Variations of wavelength ratio $\lambda_{x,H}/\lambda_{x,M}$ as a function of (a) Re_w at $Pr = 1$ and (b) Pr at $Re_w = 8600$.

this study, the wavelength ratio $\lambda_{x,H}/\lambda_{x,M}$ monotonically decreases with increasing Re_w, while $\lambda_{x,H}/\lambda_{x,M}$ exhibits a minimum around $Pr = 0.5$, indicating that the scale dissimilarity between momentum and heat transfers is most pronounced around this Prandtl number.

SUMMARY AND OUTLOOK

As described above, spectral dissimilarity is observed in all cases examined in the present study, with the exception of the lowest-Re_w case ($Re_w = 1500$, $Pr = 1$), where the flow is transitional and exhibits a spatially intermittent turbulence. The distributions of $\mathscr{E} * -uv$ and $\mathscr{E} * -v\theta$ indicate that turbulent heat transfer is associated with shorter streamwise wavelengths than turbulent momentum transfer, and such a dissimilarity between the momentum and heat transfer spectra becomes increasingly pronounced with increasing Reynolds number and attains its maximum around $Pr \approx 0.5$ within the Re_w–Pr parameter range investigated in the present study.

The instantaneous velocity and temperature fields at some representative cases are compared in Fig. 8—in the panel (a) those at $Re_w = 4300$ and 19000 with $Pr = 1$ are compared, while the panel (b) compares the cases of $Pr = 0.1$ and $Pr = 4$ at $Re_w = 8600$. Comparing the instantaneous velocity and temperature distributions in each Case R43P1 and Case R190P1 in Fig. 8(a), one can see that the temperature fields indeed exhibit finer structures as compared to the corresponding velocity fields. In the panel (b), the same tendency is indicated by the velocity and temperature fields in Case R86P01 and Case R86P4. It is interesting to note that the difference in the streamwise length scales in the velocity and temperature fields is more pronounced in Case R86P01 than in Case R86P4, although the effect of viscous diffusion is more than one order of magnitude larger than in Case R86P01.

The mechanism by which a significant disparity arises between the characteristic scales of turbulent momentum transport and turbulent heat transport remains unclear, and therefore requires further detailed investigation. Spectral analysis of the transport budget for the turbulent kinetic energy and turbulent heat flux may provide useful insights. Previous studies (Kawata & Tsukahara, 2022) have suggested that, in the transport of velocity fluctuation energy, the energy redistribution effect due to the pressure–strain correlation—prominent in relatively short-wavelength ranges—plays an important role. However, it is unclear whether a similar trend can be observed in low Pr cases, such as Pr=0.1 and Pr = 0.4, and it will be a key topic in our future studies.

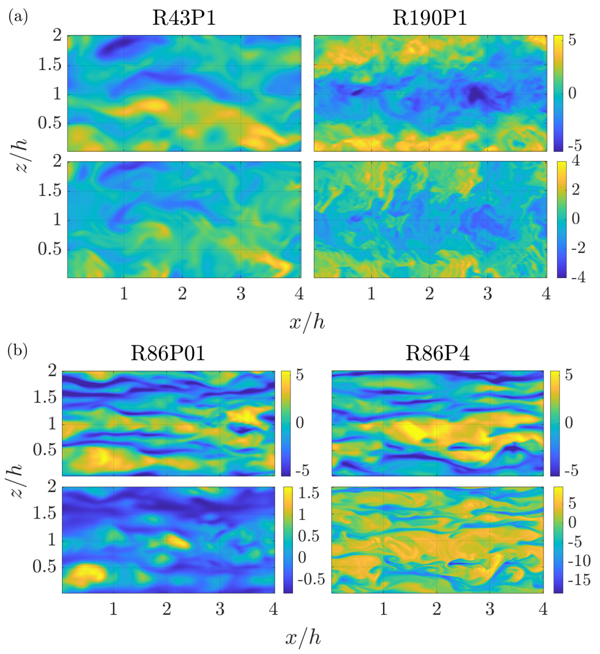

Figure 8. Instantaneous distributions of fluctuating (upper) velocity u^+ and (lower) temperature θ^+: (a) different Re_w conditions at channel centre; (b) different Pr conditions at $y \sim 0.08$ ($y^+ \sim 20$).

REFERENCES

Abe, H., Kawamura, H. & Matsuo, Y. 2004 Surface heat-flux fluctuations in a turbulent channel flow up to $re_\tau = 1020$ with $pr = 0.025$ and 0.71. *Int. J. Heat Fluid Flow* **25**, pp. 404–419.

Chiarini, A., Mauriello, M., Gatti, D. & Quadrio, M. 2022 Ascending-descending and direct-inverse cascades of Reynolds stresses in turbulent Couette flow. *J. Fluid Mech.* **930**, A9.

Cimarelli, A., De Angelis, E., Jiménez, J. & Casciola, C. M. 2016 Cascades and wall-normal fluxes in turbulent channel flows. *J. Fluid Mech.* **796**, 417–436.

Kawata, T. & Tsukahara, T. 2022 Spectral analysis on dissimilarity between the turbulent heat and momentum transport in plane Couette turbulence. *Phys. Fluids* **34**, 075135.

Lee, M. & Moser, R. D. 2019 Spectral analysis of the budget equation in turbulent channel flows at high Reynolds number. *J. Fluid Mech.* **860**, 886–938.

Mizuno, Y. 2016 Spectra of energy transport in turbulent channel flows for moderate Reynolds numbers. *J. Fluid Mech.* **805** (25), 171–187.

Tsukahara, T., Kawamura, H. & Shingai, K. 2006 DNS of turbulent Couette flow with emphasis on the large-scale structure in the core region. *J. Turbul.* **7** (19).

Tsukahara, T., Sek, Y., Kawamura, H. & Tochio, D. 2005 DNS of turbulent channel flow at very low Reynolds numbers. *In Proc: The 4th International Symposium on Turbulence and Shear Flow Phenomena* .